Journal of Physics: Conference Series **142** (2008) 012032 doi:10.1088/1742-6596/142/1/012032

Electrode geometry effects on the collection efficiency of submicron and ultra-fine dust particles in spike-plate electrostatic precipitators

D. Brocilo[1], J. Podlinski, J.S. Chang, J. Mizeraczyk, and R.D. Findlay

* McMaster University, Hamilton, Ontario, Canada and IFM Polish Academy of Science, Gdansk,Poland

E-mail: drazena@power.eng.mcmaster.ca

Abstract. The collection efficiency of electrostatic precipitators for the submicron particles ranging from 0.1 to 1 μm and ultrafine particles smaller than 0.1μm is below the requirements of new PM2.5 emission regulations. In this work, numerical and experimental studies were conducted to examine the effect of discharge and collecting electrode geometries on the ion density and electric field profiles and consequently their effect on the particle surface charge and collection efficiency. The collection efficiency prediction was based on a modified Deutsche's equation after calculation of three dimensional electric field and ion density profiles. Whereas, the particle surface charge was obtained from diffusion and field charging models. Results show that the collection efficiency of fine particles for the spike-type discharge electrode when compared to the conventional wire-type was improved. Experimental validations were conducted on a bench scale electrostatic precipitator for total and partial collection efficiency of particles ranging in size from 0.01 to 20 μm and the results indicated that the model can be effectively applied for prototype design, modification, and scale-up of collecting and discharge electrodes.

1. Introduction

Major limitation of dry-type electrostatic precipitators (ESPs) with dc energization is that the fractional penetration of 0.1 up to 1.0μm particles is typically at least an order of magnitude greater than for 10-μm particles, so that the particles that are of greatest health concern (d_p<1μm) are collected with the lowest efficiency. Therefore, in order to meet recent emission standard PM2.5 specified for submicron particulate matter less than 2.5μm in diameter, the existing ESPs have to be modified. For examples the conventional smooth wire-type discharge electrodes, characteristic for very low corona-onset voltage and high electric field near the discharge electrode but very frequent mechanical breakdowns due to the corona discharge induced vibrations, were replaced with more rigid type discharge electrodes such as rods and plates with needles and spikes. Additionally, the dry-type ESPs, may experience decreased efficiencies for high resistivity fly-ashes (above 10^{10}Ωcm), due to the initiation of back corona discharge triggered by the electrical breakdown of the dust layer at collecting plates. Based on the experimental investigations of Masuda and Mizuno [1], the collection efficiency of submicron dust particles in the presence of back corona discharge, can be reduced significantly due to the reduction in both, particle surface charge and migration velocity due to neutralization of incoming negatively polarized particles and reduction the electric field near the collecting electrode by

a positive ions created during the back-corona discharge. The Hofer and Schwab [2] experiments on rigid-plate type ESP with spikes oriented towards the collecting electrodes showed initialization of back corona discharge outside highly-packed dust-layer regions of ellipsoid shape, leading to importance of uniform ionic current profile on the collecting electrode.

Since no comprehensive numerical and experimental validations exist for rigid type discharge electrode with spikes parallel to the collecting electrode, in this work an investigation was conducted into the prediction of the electric field and ion density distribution as an integral part of a comprehensive study of the effect of discharge electrode geometry on particle charging and collection efficiency of submicron dust particles with dc energization.

2. Experimental set-up

Schematic diagrams of experimental set-ups for measurement of total and fractional penetration of particulate matter by condensation nucleation particle counter and light emitted near the discharge electrode surface by optical spectrometry and digital CCD camera systems are shown in Figure 1a. The dimensions of the spike-type discharge electrode are shown in Figure 1b.

The dust particle concentration, in terms of the number of particles per volume [#pt/m^3], was measured by the condensation nucleation particle counter (CNPC), TSI model 3010. CNPC was connected to two sampling probes over a directional valve and a particle size separation chamber PSSC. Semi-partial and partial collection efficiencies were obtained by inserting particle size separation filters in the particle separation chamber to achieve the desired particle size cut-off. While, the total collection efficiency of particulate matter, was obtained from measured data without filters.

The optical spectrometry system (OCEAN OPTICS, Model PC1000) consisting of the optical spectrometry probe (OSP), single optical fiber and spectrometer card placed in the personal computer was used. An optical fiber of 2 mm in diameter with SMA termination (SubMiniature version A) was used as a probe. The sampling rate of a spectrometer card was set to 1 kHz with an integration time of

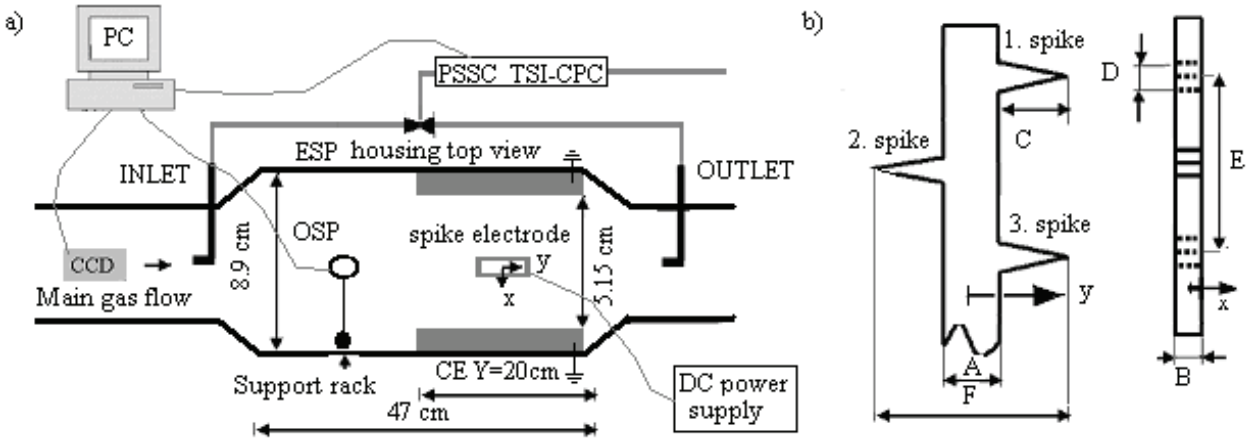

Figure 1. Schematic diagram of : (a) the experimental set-ups, and (b) dimensions of the spike-type discharge electrode where A=10 mm, B=1.5mm, C=D= 9 mm, E=64 mm.

four seconds. In order to minimize corona discharge disturbance by the OSP probe location and prevent spark-over to the probe, the OSP was mounted on the insulated support rack that allowed for the fine positioning in X and Z directions with steps of 0.5 mm. Additionally, the digital image of the corona discharge recorded by the CCD camera (Sony CCD-TRV) was compared to visible wavelengths from the optical spectrometry system to determine indirectly the spatial resolution of the optical probe. The spatial resolution of CCD system was 0.125 mm.

3. Numerical simulations

In the first section of the numerical model, collecting and discharge electrode dimensions, magnitude of dc applied voltage (V_o), main gas flow rate (Q_g), gas composition, particle size diameter ($d_p=2r_p$) and shapes were selected. In the second initialization section, the analytic approximations for the

main gas flow, Laplace's electric field, and guessed number of initial ions (Nio_g) based on electric field on the surface of discharge electrode, and predicted averaged current from the time averaged current-voltage (I-V) model were obtained. After that the Poisson's and ion transport equations with initial ion density at the surface of the discharge electrode obtained from the search algorithm were coupled in an iterative way until the solutions were self-consistent. The whole procedure can be time consuming, especially for three dimensional studies. The coupling between charged dust transport equation and Poisson's equation was not required since dust Debye number was less than 0.001, due to the small dust loading. The coupling between ion density and gas flow was not considered since the EHD number (E_{hd}) was below the value at which significant main gas flow modifications were observed ($E_{hd}<Re^2$), where Re is the flow Reynolds number. [3,4]

3.1. Ion Density *

The ion density calculations were based on the steady-state frozen chemistry with balanced source and sink term (S_{ni} - R_{ni}=0). The production of negative ions (S_{ni}) due to the electron attachment as well as the sink of negative ions (R_{ni}) due to the electron detachment or positive ion recombination is considered zero outside the ionization zone [5]. The dimensionless form of the negative ion transport equation for the case of constant ion mobility (μ_{ni}) and ion diffusion (D_{ni}) is shown in (1).

$$Ra_i\vec{u}_g\cdot\nabla^* n_{ni} - F_E n_{ni}\nabla^*\cdot\vec{\xi} - F_E\vec{\xi}\cdot\nabla^* n_{ni} - \nabla^{*2} n_{ni} = S_{ni} - R_{ni} \qquad (1)$$

where $\nabla^*=L\nabla$ is the dimensionless operator, L[m] is the characteristic length, $Ra_i=U_oL/D_{ni}$ is the dimensionless diffusion Reynolds number, F_E is dimensionless electric field number, $u_g=U_g/U_0$ is the dimensionless gas velocity, U_o[m/s] is the mean gas velocity, $n_i=N_{ni}/N_{io}$ is the ion number density ratio, N_{io} [# of ions/m^3] is the initial number density of ions, $\xi=-\nabla^*\Phi^*$ is the dimensionless electric field, $\Phi^*=\Phi/\Phi_0$ is the dimensionless electric potential ratio, $\Phi_0=F_E=eV_0/(kT)$ is the electric field number, V_0 [V] is the applied voltage, D_{ni} [m^2/s] is the ion diffusion, $e=1.602\times10^{-19}$ [C] is the charge of one electron, $k=1.381\times10^{-23}$ [J/K] is the Boltzmann constant, T [K] is the gas temperature. The ion mobility μ_{ni} is considered to be invariant to the electric field and is correlated with ion diffusion D_{ni} over Einstein's relation $\mu_{ni}= D_{ni}e/kT$.

Equation (1) is of the steady-state quasilinear second-order elliptic partial differential equation of convection-diffusion type for which the upwind differencing method [6], value at the interface is equal to the value at the grid point on the upwind side, is the well-known approach used for the formulation of terms containing ∇n_{ni}. The second term that contains the $\nabla\cdot\xi$ is usually substituted by Poisson's equation (3). The central differencing method is used for the fourth term.

The boundary conditions for the ion transport equations are usually described by the continuum conditions for which the ion density at the surface of discharge and grounded electrodes were approximately zero or order of Knudsen number ($Kn=\lambda_i/L$), where λ_i is the mean free path of ions and L is the characteristic length in this case the grounded electrode spacing. However, applying these boundary conditions introduced numerical instabilities due to the large ion density gradient near electrodes [7]. Therefore, the profile of the optical emission of the UV band (2nd positive band), that is directly proportional to the electron density and hence proportional to the negative ion distribution, was used to determine the boundary conditions.

During corona discharge, the excited nitrogen molecules $N_2(C^3\Pi_u)$ or $N_2^+(B^2\Sigma_u^+)$, produced by electron-nitrogen molecule N_2 impact, will transfer back into $N_2(B^3\Pi_g)$ or $N_2^+(X^2\Sigma_g^+)$ state by emitting photons of specific wavelength. Typical emission spectra with indicated vibration levels [8] of N_2 second positive band (N_2-2^{nd}-PB) and N_2+ first negative (N_2^+-1^{st}-NB) bands are shown in Figure 2a. Around the edges of the spike, the electrons have enough energy to produce mainly the nitrogen molecule excited ions $N_2^+(B^2\Sigma_u^+)$ and low energy electron [9]. Therefore, the maximum of visual band emission is near the spike edges, where the electric field is higher. On the other hand, $N_2(C^3\Pi_u)$ excited molecules associated with lower electron energies and electric fields are produced mainly in the center of the spike.

In this study it has been assumed that the corona discharge occurs from the surface of the spike tip at which initial number was obtained from the search algorithm. However, the profiling function A_f shown in dimensionless form (2) was obtained by fitting the experimental data from Figure 2b:

$$A_f(x') = -0.4366(x')^2 + 1 \tag{2}$$

where (x'=x/B; -0.5≤x'≤0.5) is the normalized horizontal position with respect to the length (B) of the spike tip. The boundary condition at collecting electrode is set to zero. The ion density gradient in the direction normal to the inlet, outlet, bottom and top planes of the ESP is set to zero ion density.

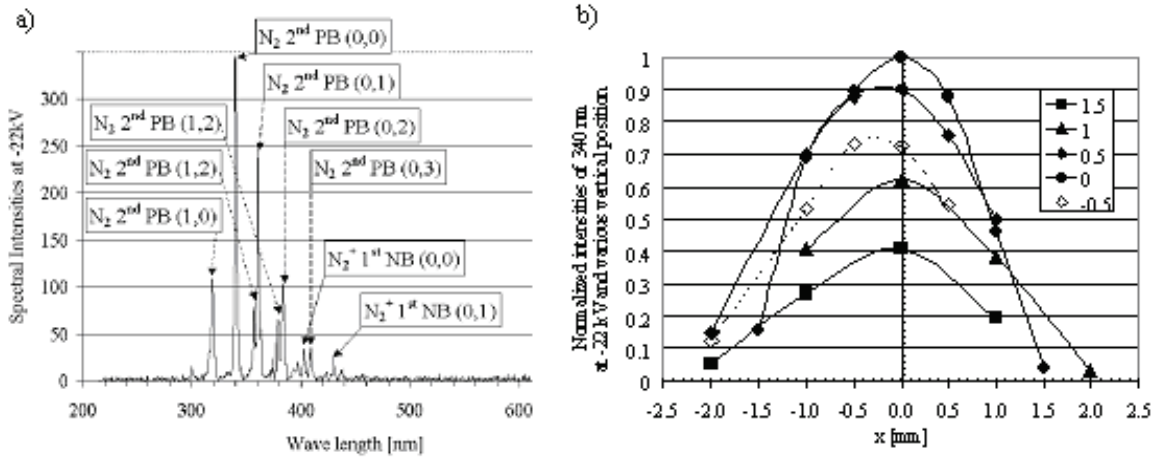

Figure. 2. (a)Typical emission spectra with indicated N_2-2^{nd}-PB and N_2^+-1^{st}-NB vibration levels, and (b) Normalized spectral intensities of N_2-2^{nd}-PB(0,0) at -22 kV relative to the spike tip locations.

3.2. Electric Potential

The electric potential is obtained from the dimensionless Poisson's equation (3),

$$\tilde{\nabla}^2 \Phi^* = -Db_i \cdot n_i / F_E \tag{3}$$

where, $Db_i=L/\lambda_{Di}$ is the Debye number, $\lambda_{Di} = \sqrt{\varepsilon kT / e^2 N_{i0}}$ [m] is Debye length, L[m] is the characteristic length and $\varepsilon=8.854\times10^{-12}$[F/m] is the electrical permittivity of free space.

The boundary conditions for dimensionless electric potential are as follows: (a) Φ*=0 at the collecting electrodes, (b) Φ*=1 at corona discharge electrode, and (c) the voltage gradient in the direction normal to the boundary at the inlet, outlet, bottom, and top plane of the ESP is zero.

3.3. Dust particle surface charge and collection efficiency calculations

Main gas velocity, electric field, and ion density profiles are passed to the cross-sectional averaging model, based on which the particle surface charge and penetration p_i were obtained in each section.

The total collection efficiency η was predicted based on the cumulative expression of Deutsche's equation,

$$\eta[\%] = 100\,(1 - \sum_{i=1}^{i=M} p_i); \qquad p_i = \exp(-(\frac{\omega_{th,i} A}{Q_g})^k); \qquad \omega_{th,i} = \frac{eN_t C_m}{6\pi\mu_g r_p} E_i \tag{4}$$

where, p_i is the cross-sectional penetration, $\omega_{th,i}$ [m/s] is the theoretical migration velocity of charged particle, E_i[V/m] is the cross-sectional averaged electric field, C_m is the Cunningham slip factor, μ_g[Pa s] is the gas viscosity, A_i[m^2] is the local dust collection surface area, and (0.5< k<1) is correction coefficient based on the dust property that in the present study was set to k=1.

The total number of elementary charges on the surface of the dust particle ($Nt=(1-\alpha)Nf+\alpha Nd$) due to the diffusion (Nd) and field charging (Nf) mechanisms for the fractional charging coefficient α of 0.5 were determined for the all three dust particle size regimes: free-molecule (Kn>10), transition (0.1<Kn<10), and continuum (Kn<0.1). The particle size regimes were determined based on the Knudsen number ($Kn=\lambda_i/r_p$) defined as the ratio between the mean free path of ions (λ_i) and the radius

of the particle (r_p) as a characteristic length. Diffusion charging for all three dust particle size regimes was based on the Chang [10] model. Particle surface charge due to the field charging mechanism was based on modified Brock-Parker [11] model in transition and free-molecule regime and Pauthenier&Moreau-Hanot [12] model in continuum regime.

4. Discussion and experimental validations

Several aspects of spike type discharge electrode geometry under varying operating conditions were evaluated and compared to the wire type discharge electrode (DE). In general, the average value of electric field in x- and y-directions increases non-uniformly with increased absolute value of applied voltage. However, when the ionic space charge effect becomes significant, the electric field near the DE surface, as well as the volume averaged value, decreases. Contour lines of ion densities at –20 kV and –25 kV at y-z plane are shown in Figures 3a and b. The numerical results show that the contour lines of ion density close to DE surface are enclosing smaller area for applied voltage of -25kV when compared to the results obtained at -20kV. This may be attributed to reduced ion mobility term due to decreased $|\xi_y|$ component of electric field near DE surface.

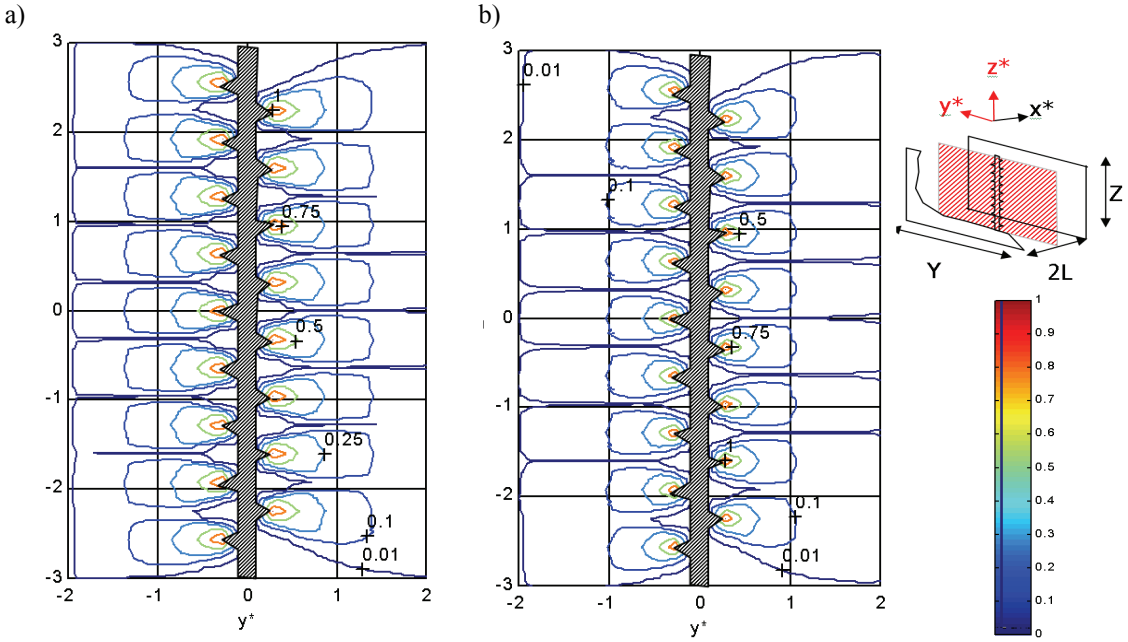

Figure. 3. Contour lines of dimensionless ion density n_{ni} (y*,z*) at x*=0 plane for (a) V_o=-20kV, N_{io}=1.69×10^{15}, Db_i^*=3.82, E_{hd}/Re^2=0.67, and (b) V_o=-25kV, N_{io}=4.08×10^{15}, Db_i^*=7.37, E_{hd}/Re^2=1.19

Predicted fractional particle collection efficiencies for spike and wire type discharge electrodes as a function of particle diameter and applied voltage, is plotted in Figure 4a. In general, the spike type discharge electrode has better collection efficiency than the wire type electrode and both electrodes have minimum efficiency for particles ranging from 0.1 to 1μm. At applied voltages of –20, –25 and –30kV, the spike-type DE has 103, 120, and 35 % higher $|\xi_x|$ component of electric field and 36, 41, and 4 % higher $|\xi_y|$ component of electric field, when compared to wire-type DE. Additionally , the volume averaged ion density of spike DE is one order of magnitude larger than that of the wire type at the same applied voltage, due to the higher discharge current. Based on the particle surface charge and cross-sectional cumulative efficiencies, the field charging mechanisms is effective only in the vicinity of DEs, due to the high electric field and ion density of surrounding area. The area of large ion density contributes more to the particle surface charge of ultrafine particles for which the charge gain due to the diffusion becomes main charging mechanism. Additionally, it has been observed that the micron size dust particles reach saturation charge limit near the first DE after which the surface charge

increases mainly due to the diffusion charging, however at very small rate. Figure 4b shows experimental validations of total collection efficiency for spike type DE. At applied voltage of *–18 kV* the model overestimates collection efficiency most probably due to the misalignment of discharge electrode, as proved by discontinuity of measured current-voltage at that particular voltage level. For applied voltages of *-20 kV and - 22 kV,* the model agrees within *1.5 and 4 %.* However, for the applied voltage of *-26 kV,* the model overestimates collection efficiency by *60 %* . Since the measured current-voltage curve did not indicates any problem due to the suspected electrode misalignment, it is believed that in addition to the present ionic space charge effect, one of the reasons for impaired collection efficiency might be due to the EHD induced secondary flow, too. When the ratio of E_{hd} *and* Re^2 becomes larger than one significant main gas flow modifications as well as the re-entrainment of collected dust particles might occur.

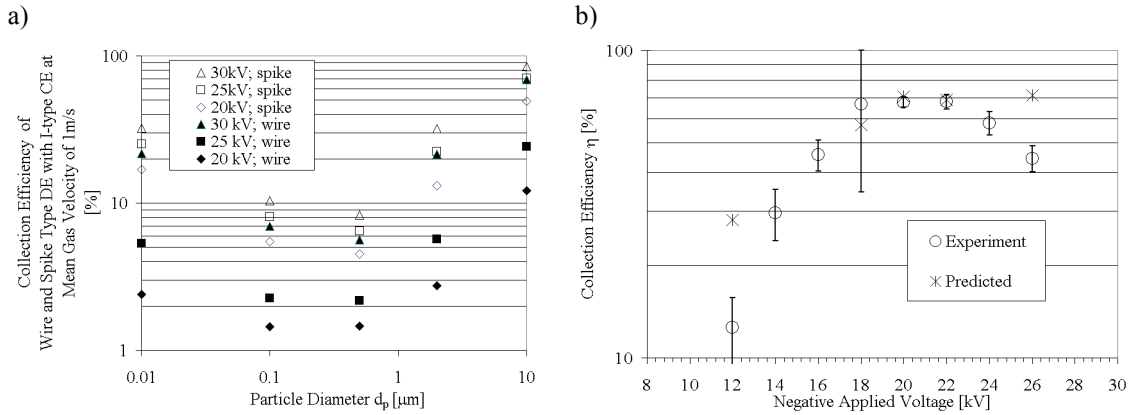

Figure. 4. (a) Particle collection efficiencies for spike and wire-type DEs as a function of applied voltages at Q_g=108 m^3/h. (b) Measured versus predicted total dust collection efficiency of spike-type DE at Q_g=17 m^3/h.

5. Conclusions

Based on the numerical results and experimental validations, the following concluding remarks were obtained: (a) For given operating and geometry conditions, space charge effect due to the ions can be observed when D_{bi}^* is larger than 7. (b) Field charging mechanisms is still important in the area close to the discharge electrode surface for submicron dust particles. (c) Experimental validations of particles ranging in size from 0.01 to 20μm proved the model to be effective for collection efficiency predictions when EHD number versus Reynolds number squared is below one, (d) In order to distinct between direct and indirect effects of the EHD flow further studies of its effect on particle surface charging, particle convection, and re-entrainment of already collected dust particles are required.

References

[1] S. Masuda and A. Mizuno, *Journal of Electrostatics*, vol. 4, pp. 35-52, 1977.
[2] B. Hoferer and A.J. Schwab, 2000 Conf. on El. Insulation and Dielectric Phenomena, pp. 93-96
[3] IEEE-DEIS-EHD Tech. Committee , IEEE Trans. on Dielectrics and El. Insul., 10, 3-6, 2003.
[4] Podlinski et al. *Journal of Electrostatics,* No. 64, 2006, pp. 259-262.
[5] D. Brocilo et al., *Proc. of 8th Int. Conf. on Electrostatic Precipitation*, May 2001, vol. II, A4-3.
[6] J.S. Chang et al., *Proc. Int. Conf. Comp. Fluid Dynamics, K. Oshima,* Ed. vol. 1, pp. 422-434.
[7] I. Gallimberti, *Journal of Electrostatics*, vol. 43, pp. 219-249, 1988.
[8] A.A. Yastrebov, *Soviet Phys.-Tech. Phys,* vol. 17, pp. 638-645, 1972.
[9] J. S. Chang and A. Kwan, *ESA-IEJ Proceedings*, Press Morgan Hill, June 1998, pp. 390-407.
[10] J.S. Chang, J. Aerosol Sci, vol. 12, pp. 19-19-26, 1981.
[11] J.R. Brock, J. Applied Phys., vol. 41, pp. 1940-1940-1944, 1970.
[12] M.M. Pauthenier and M. Moreau-Hanot, J Phys. Radium, vol. 7, pp. 590, 1932.